ELSEVIER

Nuclear Physics A682 (2001) 1c–11c

NUCLEAR PHYSICS A

www.elsevier.nl/locate/npe

# Collective rotational motion in the N=Z nucleus $^{36}$Ar

C.E. Svensson[a], A.O. Macchiavelli[a], A. Juodagalvis[b], A. Poves[c], I. Ragnarsson[b], S. Åberg[b], D.E. Appelbe[d], R.A.E. Austin[d], C. Baktash[e], G.C. Ball[f], M.P. Carpenter[g], E. Caurier[h], R.M. Clark[a], M. Cromaz[a], M.A. Deleplanque[a], R.M. Diamond[a], P. Fallon[a], M. Furlotti[i], A. Galindo-Uribarri[e], R.V.F. Janssens[g], G.J. Lane[a], I.Y. Lee[a], M. Lipoglavsek[e], F. Nowacki[j], S.D. Paul[e], D.C. Radford[e], D.G. Sarantites[i], D. Seweryniak[g], F.S. Stephens[a], V. Tomov[i], K. Vetter[a], D. Ward[a], and C.H. Yu[e]

[a]Nuclear Science Division, Lawrence Berkeley National Laboratory, Berkeley, California
[b]Department of Mathematical Physics, Lund Institute of Technology, Lund, Sweden
[c]Departamento de Física Teórica, Universidad Autónoma de Madrid, Madrid, Spain
[d]Department of Physics and Astronomy, McMaster University, Hamilton, Canada
[e]Physics Division, Oak Ridge National Laboratory, Oak Ridge, Tennessee
[f]TRIUMF, 4004 Wesbrook Mall, Vancouver, Canada
[g]Argonne National Laboratory, Argonne, Illinois
[h]Institut de Recherches Subatomiques, Université Louis Pasteur, Strasbourg, France
[i]Chemistry Department, Washington University, St. Louis, Missouri
[j]Laboratoire de Physique Theorique, Université Louis Pasteur, Strasbourg, France

A superdeformed rotational band has been identified in the $N = Z$ nucleus $^{36}$Ar, firmly linked to known low-spin states, and observed to its high-spin termination at $I^{\pi} = 16^{+}$. Lifetime measurements by the Doppler shift attenuation method establish a large low-spin deformation ($\beta_2 \approx 0.46$) and a decrease in the collectivity as the band approaches termination. Comparisons with cranked Nilsson-Strutinsky and large-scale spherical shell model calculations lead to a consistent description of the band based on a configuration in which four particles are promoted to the $pf$ shell. With two major shells active for both protons and neutrons, yet a valence space dimension small enough to be approached from the shell model perspective, this band offers an excellent opportunity to investigate the microscopic structure of collective rotational motion in nuclei.

## 1. INTRODUCTION

The microscopic description of collective motion in the many-nucleon system is a fundamental goal of nuclear structure physics. Progress in this direction is closely linked with the identification of the symmetry properties of the underlying microscopic Hamiltonian. In the first half of the *sd* shell, for example, the degeneracies of the harmonic oscillator potential remain approximately valid and the relationship between the deformed intrinsic states of rotors like $^{20}$Ne and $^{24}$Mg and the laboratory-frame shell-model description of these nuclei was established by Elliot's SU(3) model more than forty years ago [1]. In heavier nuclei, however, the oscillator SU(3) symmetry is destroyed by the strong spin-orbit

0375-9474/01/$ – see front matter 
PII S0375-9474(00)00615-1

interaction. Furthermore, a direct shell-model approach to rotational motion in these nuclei would require diagonalizations in spaces spanned by two major shells for both protons and neutrons [2], far beyond current computational capabilities. Considerable effort has therefore been devoted to the identification of the approximate symmetries which enable a shell-model description of collective rotation within an appropriately truncated model space (cf. [3,4] and references therein). Clearly, it is desirable to investigate the validity of such approaches in cases where the valence space is large enough for collective rotation to develop, yet remains small enough for exact shell-model diagonalization. Much progress in this direction, both experimental [5–7] and theoretical [8–13], has recently been made in the study of the deformed $pf$-shell nucleus $^{48}$Cr. However, rotors like $^{48}$Cr, $^{20}$Ne, and $^{24}$Mg are exceptional, in that only a single-major shell is active. Here we discuss the identification [14] of a superdeformed (SD) rotational band in the $N = Z$ nucleus $^{36}$Ar which enables an extension of these studies of the microscopic structure of collective rotation to a case where, in analogy with rotational motion in heavier nuclei, two major shells are active for both protons and neutrons.

## 2. EXPERIMENTS

High-spin states in $^{36}$Ar were studied via the $^{24}$Mg($^{20}$Ne,2$\alpha$)$^{36}$Ar fusion-evaporation reaction in two experiments. In each case, a $\sim$ 2 pnA 80-MeV $^{20}$Ne beam was provided by the ATLAS facility at Argonne National Laboratory. In the first experiment, a self-supporting 440 $\mu$g/cm$^2$ $^{24}$Mg target was used, while in the second experiment lifetimes were measured by the Doppler shift attenuation method with a 416 $\mu$g/cm$^2$ $^{24}$Mg target deposited on a 11.75 mg/cm$^2$ Au backing. In both experiments, $\gamma$ rays were detected with 101 HPGe detectors of the Gammasphere array [15] in coincidence with charged particles detected and identified with the Microball [16], a $4\pi$ array of 95 CsI(Tl) scintillators. The Hevimet collimators were removed from in front of the BGO Compton suppression shields of the HPGe detectors to enable total $\gamma$-ray energy and multiplicity measurements for each event [17]. Clean selection of $^{36}$Ar events was achieved by requiring the detection of two alpha particles in the Microball in combination with a total detected $\gamma$-ray plus charged-particle energy consistent with the $Q$-value for the 2$\alpha$ evaporation channel [18]. Totals of 775 million and 827 million particle-$\gamma$-$\gamma$-$\gamma$ and higher-fold coincidence events were recorded in the first and second experiments, respectively.

## 3. RESULTS AND DISCUSSION

The $\gamma$-ray spectrum from the thin-target experiment obtained by summing coincidence gates set on all members of the superdeformed band identified in $^{36}$Ar is shown in Fig. 1. A partial decay scheme for $^{36}$Ar, showing states relevant to the decay of the SD band, is presented in Fig. 2. As indicated in Fig. 2, the high-energy transitions denoted by diamonds in Fig. 1 firmly link the SD band to known low-spin states in $^{36}$Ar. For example, Figure 2 a) shows a spectrum of the band obtained with a single coincidence gate set on the 4950 keV linking transition. Angular distribution measurements [14] determine stretched-$E2$ multipolarity for these high-energy linking transitions, as well as for all of the in-band transitions, and establish the spins and parities indicated in Fig. 2. The excellent rotational behavior of the band up to the backbending at $I^\pi = 10^+$ is illustrated

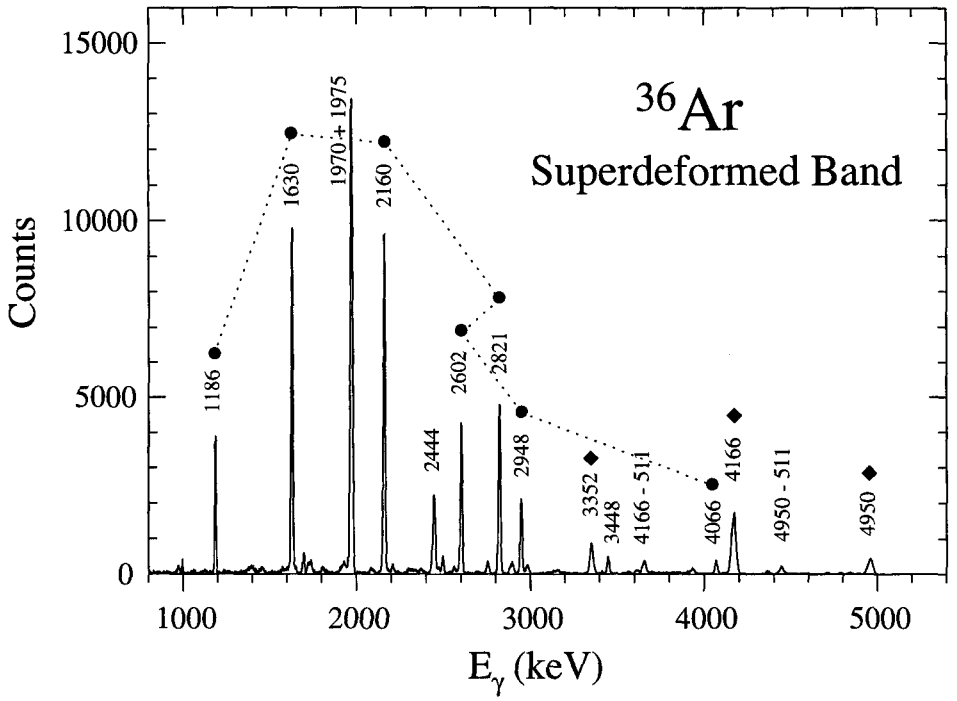


Figure 1. Gamma-ray spectrum obtained by summing coincidence gates set on all transitions in the superdeformed band (circles). Diamonds indicate linking transitions connecting the band to low-spin states in $^{36}$Ar.

by the linear increase in angular momentum with rotational frequency ($\gamma$-ray energy) shown in Fig. 2 b). Strongly enhanced in-band transitions are also suggested by the low-spin branching ratios, which imply large in-band to decay-out $B(E2)$ ratios ($148 \pm 6$ and $86 \pm 4$ for the $4^+$ and $6^+$ states of the band, respectively). Although, as expected from $\gamma$-ray energetics, in-band decay by a 622 keV transition to the previously known ($0^+$) state at 4329 keV [19] was not observed in the present experiments, this state is presumed to be the SD bandhead based on the regular rotational spacing.

A highly-deformed band in $^{36}$Ar, in which four $pf$-shell orbitals are occupied, is expected based on the gap in the single-particle energy levels of the Nilsson diagram at deformation $\varepsilon_2 \sim 0.4$ for particle numbers $N, Z = 18$ (cf. Fig. 2 in Ref. [20]). We have confirmed this interpretation of the observed SD band by carrying out detailed theoretical analyses of $^{36}$Ar employing both the configuration-dependent cranked Nilsson-Strutinsky (CNS) approach [21,22] and large-scale ($s_{1/2}d_{3/2}$)-$pf$ spherical shell model (SM) calculations with the diagonalization code ANTOINE [23]. Pairing correlations were neglected in the former, while the latter used an effective interaction based on that of Ref. [24], with the effective single-particle energies modified to account for the truncation of the full $sd$ shell. As

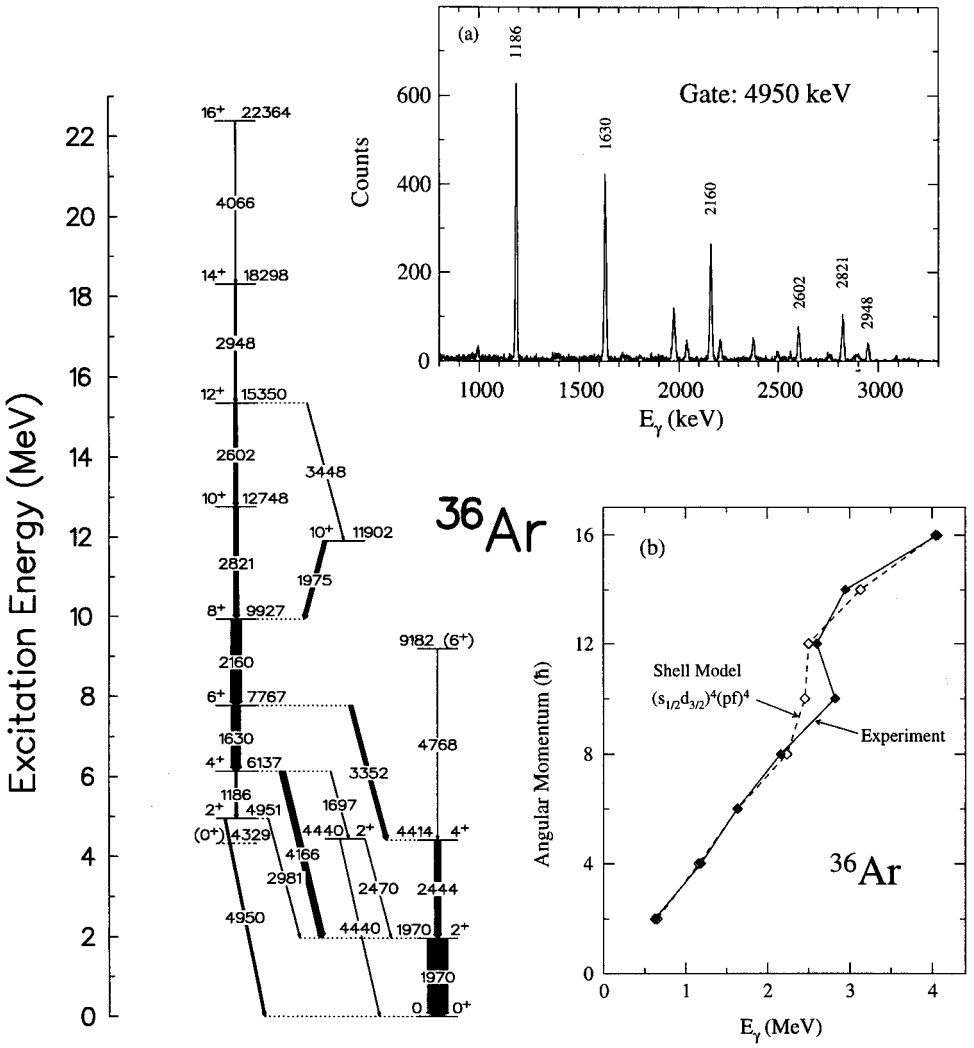


Figure 2. Partial decay scheme for $^{36}$Ar showing the superdeformed band (left). Transition and level energies are given to the nearest keV and arrow widths are proportional to the transition intensities. The upper inset shows a spectrum of the band obtained with a single gate set on the 4950 keV linking transition. The "backbending" plot for the SD band is compared with the results of spherical shell model calculations in the lower inset.

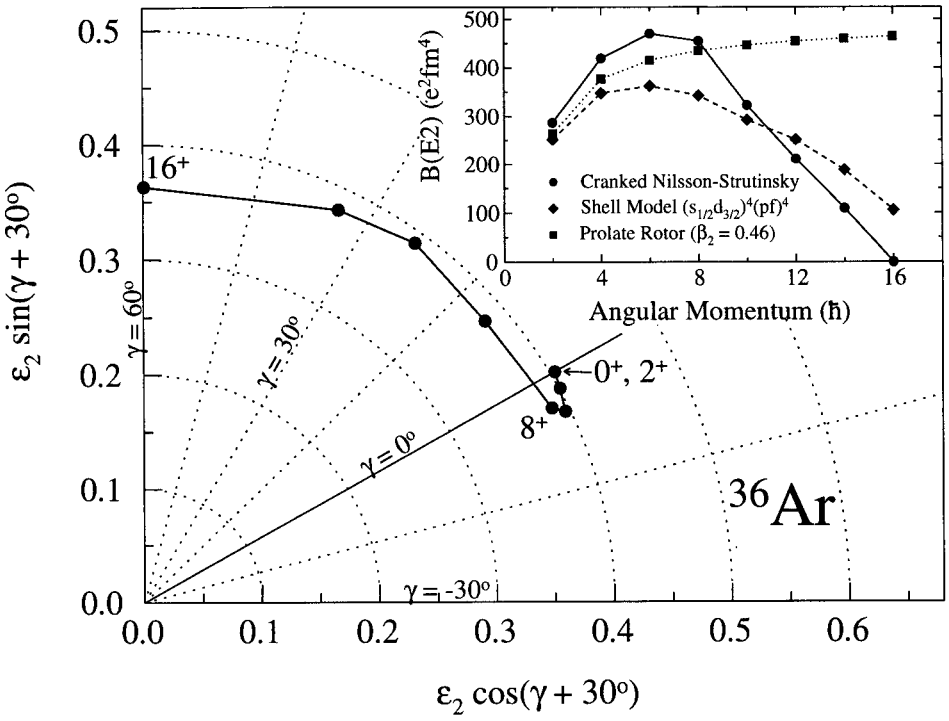


Figure 3. Calculated trajectory in the $(\varepsilon_2,\gamma)$ deformation plane for the $(pf)^4$ band in $^{36}$Ar. The inset shows the corresponding $B(E2; I \rightarrow I-2)$ values from the cranked Nilsson-Strutinsky (circles) and spherical shell model (diamonds) calculations. The $B(E2)$'s for a fixed prolate deformation $\beta_2 = 0.46$ are also shown for comparison (squares).

detailed in Ref. [14], these calculations provide an excellent description of the observed band and firmly establish the $(pf)^4$ configuration assignment suggested by the Nilsson diagram. Here we simply illustrate, in Fig. 2 (b), the impressive agreement between the SM calculations for this configuration and the energetic properties of the band, noting that even the slight discrepancy for the $10^+$ state can, at least partially, be accounted for by an interaction with the nearby yrast $10^+$ state at 11902 keV (predicted to belong to the $(pf)^2$ configuration in both calculations [14]).

The predicted equilibrium deformations for the $(pf)^4$ configuration from the CNS calculations are shown as a function of angular momentum in Fig. 3. At low-spin a prolate ($\gamma = 0°$) shape with deformation $\varepsilon_2 \sim 0.40$ ($\beta_2 \sim 0.47$) is predicted, and this intrinsic shape remains approximately constant up to $I \sim 8\hbar$. At higher spins, the CNS calculations predict a gradual shape change with $\gamma$ smoothly increasing at roughly constant $\varepsilon_2$, terminating at $I^\pi = 16^+$ in a fully-aligned oblate ($\gamma = 60°$) state. Assuming the rotational model, the $B(E2)$ values corresponding to these equilibrium deformations are shown by

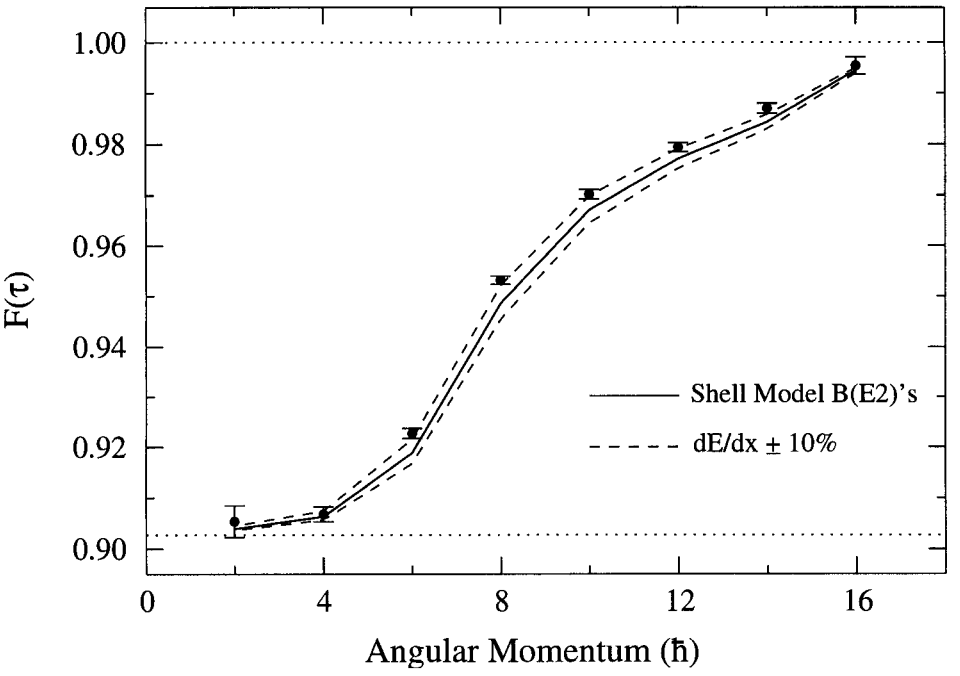


Figure 4. Fractional Doppler shifts measured for the transitions in the $^{36}$Ar superdeformed band (circles). The solid line shows the $F(\tau)$ values calculated assuming the shell-model $B(E2)$ values, and the dashed lines the corresponding values obtained by scaling the stopping powers by $\pm 10\%$. The dotted lines at $F = 1.00$ and $F = 0.903$ represent the full Doppler shift and mean value for recoils which have exited the thin-target, respectively.

the circles in the inset in Fig. 3. At low spins, the CNS prediction of an excursion to negative $\gamma$ values leads to $B(E2)$ values slightly larger than those of a $\beta_2 = 0.47$ prolate rotor, while at high spin the transition to an oblate state implies a loss of collectivity and the rotational $B(E2)$ vanishes at the terminating state. Also shown in Fig. 3 are the $B(E2)$ values predicted by the shell model calculations with core-polarization taken into account by means of effective charges $q_\pi = 1.5$ and $q_\nu = 0.5$. The general trend is in reasonable agreement with the CNS predictions. However, the spin-dependence is weaker in the SM calculations, where the predicted $B(E2)$'s are smaller at low spins but larger at high spins, and remain substantial even at the terminating state.

In order to test the quadrupole properties predicted by the two models, we have measured lifetimes in the $^{36}$Ar SD band. For $I \geq 8\hbar$, the high transition energies lead to state lifetimes which are short compared to the mean time (of order 100 fs) taken by the recoils to exit the thin $^{24}$Mg target. Lifetimes for these states were therefore measured

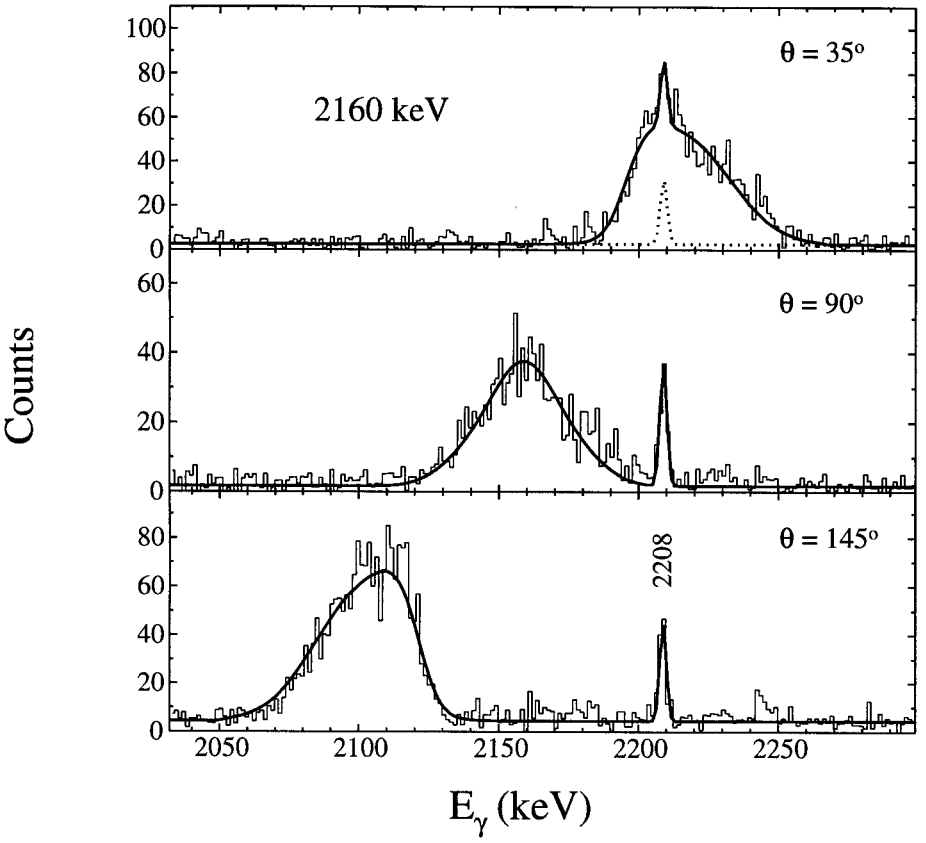


Figure 5. Doppler-shift attenuation lineshape analysis for the 2160 keV $8^+_{SD} \rightarrow 6^+_{SD}$ transition. The stopped peak at 2208 keV is the $3^-_1 \rightarrow 2^+_1$ transition in $^{36}$Ar.

by the thin-target Doppler shift attenuation method [25]. The measured fraction $F(\tau)$ of the full Doppler shift for each transition in the SD band is shown in Fig. 4. The solid curve in this figure shows the $F(\tau)$ values calculated with the shell-model $B(E2)$ values and stopping powers for $^{36}$Ar in $^{24}$Mg from the SRIM-2000 code [26]. While the trend of the experimental data is well reproduced, the measured $F(\tau)$ values at intermediate spins are clearly larger than the calculated values. This implies that either the shell model $B(E2)$'s are smaller than the experimental values or that the stopping powers used in the calculations were too large, or possibly both. In order to investigate the sensitivity to uncertainties in the stopping powers, we have repeated the calculations with the SRIM-2000 values scaled by $\pm 10\%$. The results are shown by the dashed curves in Fig. 4, where it is seen that agreement between the experimental $F(\tau)$ values and the shell-model $B(E2)$'s can just be achieved at the lower limit of this stopping power range.

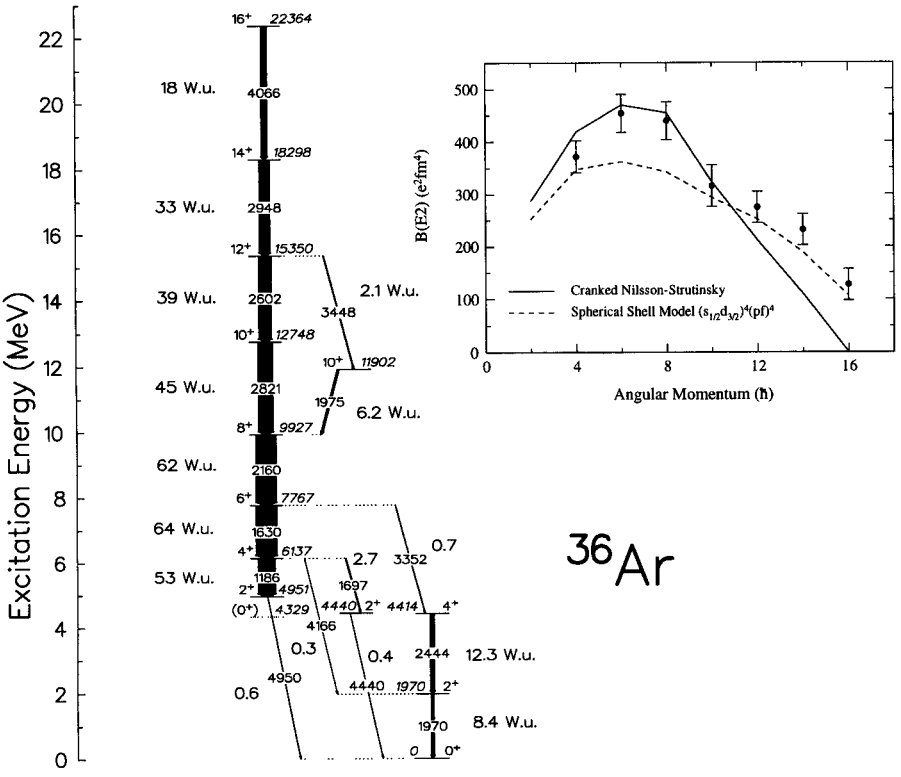


Figure 6. Partial decay scheme for $^{36}$Ar showing the superdeformed band. The arrow widths are proportional to the $B(E2)$ values, which are also given in Weisskopf units beside each transition. The inset compares the experimental B(E2) values with the predictions of the cranked Nilsson-Strutinsky (solid line) and shell model (dashed line) calculations.

For the lower-spin states in the $^{36}$Ar SD band, the cumulative lifetime becomes long enough that a substantial fraction of the decays occur after the recoils have exited the $^{24}$Mg target. For these states, additional lifetime information was obtained from the second experiment in which the recoils stopped in the Au target backing. The lineshapes of these transitions were simultaneously fit at forward ($\overline{\theta} = 35°$), middle ($\theta = 90°$), and backward ($\overline{\theta} = 145°$) angles relative to the beam axis using a version of the LINESHAPE code [27] modified to account for both the broad initial $^{36}$Ar recoil momentum distribution produced by the evaporation of two alpha particles, and the substantial bias in this distribution produced by the angle-dependent alpha particle detection efficiency. The quality of the fits to the data obtained by this procedure is illustrated for the 2160 keV $8^+ \rightarrow 6^+$ transition in the SD band in Fig. 5. A detailed discussion of these results will be given in a forthcoming publication [28].

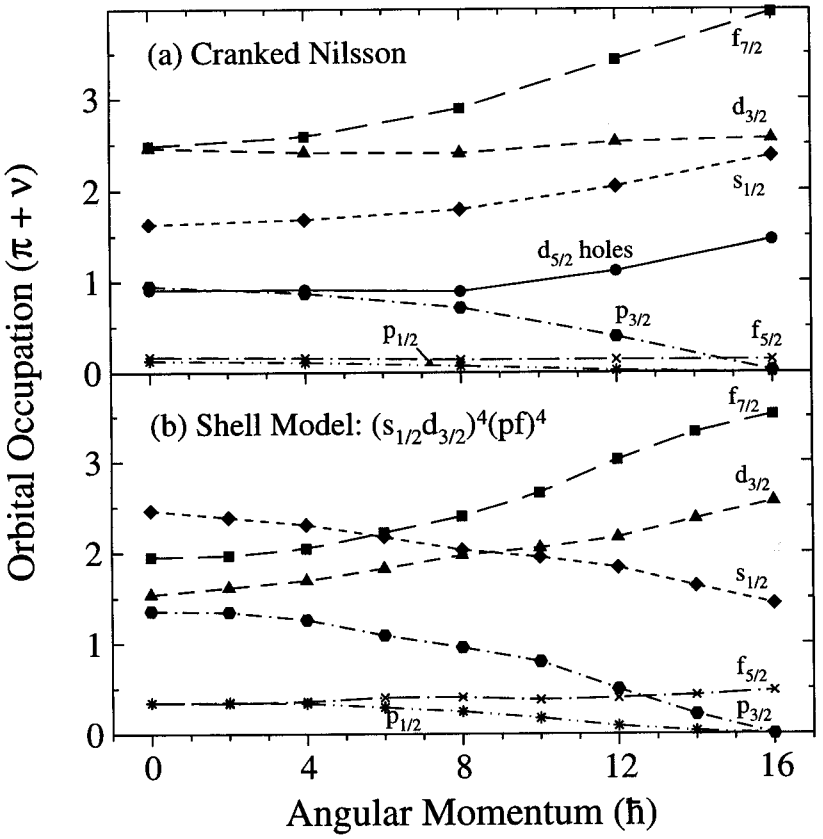


Figure 7. Occupancies of spherical $j$-shells in the $^{36}$Ar superdeformed band from (a) cranked Nilsson-Strutinsky and (b) spherical shell model calculations. In the Nilsson calculations there are also small occupancies in higher major shells.

The $B(E2)$ values from both the thin- and backed-target measurements are summarized in Fig. 6. The large $B(E2)$'s connecting the low-spin members of the SD band, corresponding to $\beta_2 \approx 0.46$ for a prolate shape, are clearly seen in this representation of the level scheme. At high-spin the $B(E2)$ values decrease, but, in agreement with the shell model calculations, remain substantial ($\sim$ 18 Weisskopf units) even at the terminating state. The discrepancy with the CNS predictions at high spin is not unexpected, as fluctuations about the equilibrium deformations of Fig. 3 become important [13] as the rotational $B(E2)$ values become small. For the low-spin states, the experimental $B(E2)$'s are in good agreement with the CNS calculations, but are clearly larger than the SM predictions for the $I^\pi = 6^+$ and $8^+$ states. In order to investigate possible sources of this discrepancy, it is interesting to compare the detailed structure of the wavefunctions for the SD states in the two models.

In Fig. 7 we present the spherical $j$-shell occupancies in the SD band from the two calculations. The CNS values were obtained according to the formalism of Ref. [29]. Firstly, we note that the relatively constant occupancies at low spin validates the concept of a rotational band built on a fixed intrinsic state. At higher spins, the increasingly rapid changes in the subshell occupancies are associated with changes in the deformation of this intrinsic state, as illustrated in Fig. 3. The $pf$-shell occupancies predicted by the two calculations exhibit very similar trends, with the SM calculation yielding slightly higher absolute occupancies in the upper $pf$ orbitals. This close similarity reflects the dominance of quadrupole deformation in determining the structure of the wavefunction for this band, with the full shell-model treatment of all correlations, in particular pairing, leading to only a slight increase in the subshell mixing compared to the deformation-related effects accounted for in the CNS calculations. In the $sd$-shell it was necessary to truncate the shell-model space to $(s_{1/2}d_{3/2})$, although, as shown in Fig. 7 a), the CNS calculations indicate a substantial $d_{5/2}$-hole contribution to the wavefunction. The excellent agreement between the SM calculations and the energetic properties of the band shown in Fig. 2 b) implies that the influence of such $d_{5/2}$ holes on the moment of inertia has been effectively subsumed in the 1 MeV lowering of the $s_{1/2}$ single-particle energy performed to obtain the correct spectrum for $^{29}$Si in the truncated space. The possibility remains, however, that the contribution of such $d_{5/2}$ holes to the quadrupole moment has not been fully accounted for. It is noteworthy that the intrinsic quadrupole moment $Q_0 = 113\,e\,\mathrm{fm}^2$, deduced from either the shell-model spectroscopic quadrupole moments or the calculated $B(E2)$ values connecting low-spin members of the band, already represents 80% of the maximum possible in the full $(sd)^{16}(pf)^4$ space (as attained in the unrealistic SU(3) limit). Nevertheless, a 5–10% increase in the quadrupole moment resulting from inclusion of the $d_{5/2}$-hole component in the shell-model wavefunction is certainly plausible. This corresponds to a 10–20% increase in the $B(E2)$ values which, as seen in the inset in Fig. 6, would considerably improve the agreement between the SM and experimental results. Clearly, a detailed study of the role of the $d_{5/2}$ orbital, perhaps by a full $sd$-$pf$ diagonalization by Monte Carlo techniques (cf. Ref. [30]), would be highly desirable in order to obtain a complete description of the microscopic structure of this highly collective rotational band.

## 4. CONCLUSIONS

A superdeformed rotational band has been identified in the $N = Z$ nucleus $^{36}$Ar. As shown in Fig. 6, spins, parities, excitation energies, and in-band, as well as out-of-band, $B(E2)$ values have been measured throughout the band, providing essentially complete spectroscopic data for these highly collective rotational states. While large-scale $(s_{1/2}d_{3/2})^4(pf)^4$ shell model calculations provide an impressive description of the energetic properties of the band, they underestimate the low-spin $B(E2)$ values, perhaps indicating a non-negligible contribution of $d_{5/2}$ holes to the quadrupole moment. With two major shells active for both protons and neutrons, yet a valence space dimension small enough to be approached from the shell-model perspective, this band offers an excellent opportunity for further studies of the microscopic description of collective rotational motion in nuclei.

## ACKNOWLEDGEMENTS

This work has been partially supported by the D.O.E. under Contracts DE-AC03–76SF00098, W-31-109-ENG-38, DE-AC05-96OR22464, and DE-FG05-88ER40406, the Swedish Institute, NFR (Sweden), DGES (Spain) under Grant No. PB96-53, NSERC (Canada), and IN2P3 (France).

## REFERENCES

1. J.P. Elliott, Proc. R. Soc. London 245, 128 (1958); 245, 562 (1958).
2. K. Kumar and M. Baranger, Nucl. Phys. A110, 529 (1968).
3. A.P. Zuker *et al.*, Phys. Rev. C 52, R1741 (1995).
4. C. Vargas, *et al.*, Phys. Rev. C 61, 031301(R) (2000).
5. J.A. Cameron *et al.*, Phys. Lett. B 387, 266 (1996).
6. S.M. Lenzi *et al.*, Z. Phys. A 354, 117 (1996).
7. F. Brandolini *et al.*, Nucl. Phys. A642, 387 (1998).
8. E. Caurier *et al.*, Phys. Rev. C 50, 225 (1994).
9. E. Caurier *et al.*, Phys. Rev. Lett. 75, 2466 (1995).
10. A. Juodagalvis and S. Åberg, Phys. Lett. B 428, 227 (1998);
11. A. Poves, J. Phys. G 25, 589 (1999).
12. K. Hara, Y. Sun, and T. Mizusaki, Phys. Rev. Lett. 83, 1922 (1999).
13. A. Juodagalvis, I. Ragnarsson, and S. Åberg, Phys. Lett. B 477, 66 (2000).
14. C.E. Svensson *et al.*, Phys. Rev. Lett. 85 (2000), (in press).
15. I.-Y. Lee, Nucl. Phys. A520, 641c (1990).
16. D.G. Sarantites *et al.*, Nucl. Instrum. Methods Phys. Res., Sect. A 381, 418 (1996).
17. M. Devlin *et al.*, Nucl. Instrum. Methods Phys. Res., Sect. A 383, 506 (1996).
18. C.E. Svensson *et al.*, Nucl. Instrum. Methods Phys. Res., Sect. A 396, 228 (1997).
19. P.M. Johnson, M.A. Meyer, and D. Reitmann, Nucl. Phys. A218, 333 (1974).
20. D.M. Headly, R.K. Sheline, and I. Ragnarsson, Phys. Rev. C 49, 222 (1994).
21. T. Bengtsson and I. Ragnarsson, Nucl. Phys. A436, 14 (1985).
22. A.V. Afanasjev and I. Ragnarsson, Nucl. Phys. A591, 387 (1995).
23. E. Caurier, computer code ANTOINE, Strasbourg (1989).
24. J. Retamosa *et al.*, Phys. Rev. C 55, 1266 (1997).
25. B. Cederwall *et al.*, Nucl. Instrum. Methods Phys. Res., Sect. A 354, 591 (1995).
26. J.F. Ziegler, http://www.research.ibm.com/ionbeams.
27. J.C. Wells *et al.*, ORNL Physics Division Progress Report, ORNL-6689 (1991).
28. C.E. Svensson *et al.*, to be published.
29. R.K. Sheline *et al.*, J. Phys. G 14, 1201 (1988).
30. T. Otsuka, M. Honma, and T. Mizusaki, Phys. Rev. Lett. 81, 1588 (1998).